metals

MDPI

Article

Effect of Nb Content on the Microstructure and Impact Toughness of High-Strength Pipeline Steel

Jinxing Jiang [1,2], Zhongde Zhang [3], Kai Guo [3], Yingping Guan [1], Liangzeng Yuan [3] and Qingfeng Wang [3,*]

[1] School of Mechanical Engineering, Yanshan University, Qinhuangdao 066004, China
[2] Plate Business Department, Nanjing Iron & Steel United Co., Ltd., Nanjing 210035, China
[3] Laboratory of Metastable Materials Science and Technology, Yanshan University, Qinhuangdao 066004, China; yuanlzh@163.com (L.Y.)
* Correspondence: wqf67@ysu.edu.cn; Tel.: +86-335-2039067

Abstract: In this study, X80 pipeline steel is prepared with different Nb contents through the thermo-mechanically controlled rolling process. The effects of using two different Nb contents on the impact toughness and microstructure of the pipeline steel are examined using various experimental techniques. The results show that with the increase in Nb content, the transformation temperature Ar_3 decreases, and the nucleation and growth of bainitic ferrite with lath features (LB) are promoted, while those of granular bainite (GB) are inhibited. In addition, the stability of the austenite phase increases with the increase in Nb content. Therefore, the volume fractions of LB and martensite–austenite (M/A) constituents increase, while the proportion of high-angle grain boundaries (HAGBs) decreases. The impact energy of pipeline steel at −45 °C is closely related to the Nb content. Specifically, the impact energy decreases from 217 J at 0.05 wt.% Nb to 88 J at 0.08 wt.% Nb. The cracks are preferentially formed near the M/A constituents, and the HAGBs significantly inhibit the crack propagation. The steel with 0.05 wt.% Nb has a lower content of M/A constituents and a higher proportion of HAGBs than the one with 0.08 wt.% Nb. In addition, as the Nb content increases, the crack initiation energy and the crack propagation energy decrease. Thus, the 0.05 wt.% Nb steel has a higher low-temperature impact energy.

Keywords: pipeline steel; microalloying; microstructure; impact toughness

Citation: Jiang, J.; Zhang, Z.; Guo, K.; Guan, Y.; Yuan, L.; Wang, Q. Effect of Nb Content on the Microstructure and Impact Toughness of High-Strength Pipeline Steel. *Metals* **2024**, *14*, 42. https://doi.org/10.3390/met14010042

Academic Editors: Dong-Woo Suh and Heung Nam Han

Received: 28 October 2023
Revised: 21 December 2023
Accepted: 26 December 2023
Published: 29 December 2023

1. Introduction

With the rapid economic development and the continuously increasing global oil demand, pipelines have become the preferential mode of oil and natural gas transportation. At the same time, due to the complex geological conditions of oil and gas wells, more stringent requirements are being imposed on the mechanical performance of pipeline steel, especially its low-temperature fracture resistance [1–5]. Owing to its excellent comprehensive mechanical properties, X80 grade steel is commonly used in the construction of oil and natural gas pipelines. The composition of pipeline steel can significantly alter its microstructure and crystal texture, thereby affecting its low-temperature fracture resistance [6]. Therefore, it is important to consider the impact of alloy elements on the final mechanical properties. The microstructure of conventional X80 pipeline steel has a low-carbon bainite structure, including polygonal ferrite (PF), granular bainite (GB), bainitic ferrite with lath features (LB), and martensite–austenite (M/A) constituents [6–9], while the main elements affecting the transformation behavior and microstructure of high-strength pipeline steel are Mo, Nb, B, Ni, etc. [10,11].

It has been reported that with the increase in dissolved Nb content, the recrystallization temperature of austenite phase increases and initial austenite grain size decreases [6]. Therefore, the production of high-performance pipeline steel can reduce the use of Mo elements as well as the cost of steel plates. The dissolved Nb in the austenite phase can reduce the phase transition temperature, thereby refining the alloy microstructure [8]. Sun

et al. showed that Nb dissolved in austenite enhanced the strength of tempered forged steel due to its excellent solid solution strengthening effect [9]. Bai et al. showed that compared to Ti-Mo steel, Nb-Mo steel exhibited a finer microstructure and better low-temperature toughness [10]. Wu examined the relationship between the alloy elements and the strength and impact toughness of X80 pipeline steel, and the results showed that with an increase in Nb content, both the strength and impact toughness increased [11]. On the other hand, Chen studied the effect of Nb on the mechanical properties of the heat affected zone (HAZ) of X80 pipeline steel, and the results showed that a high Nb content reduced the impact toughness of pipeline steel [12]. Therefore, a clear consensus has still not been achieved on the influence of Nb on the low-temperature toughness of steel. Although several researchers have examined the influence of Nb content on the phase transformation and properties of pipeline steel [13–18], they have mainly focused on the phase transformation points, microstructural composition, and grain size, and the inherent structural factors that affect the toughness have been mostly ignored.

In this study, X80 grade pipeline steel is prepared with two different Nb contents, and the effects of Nb content on the phase transformation, microstructure, and properties of X80 grade pipeline steel are comprehensively analyzed. In particular, the microstructural evolution under different Nb contents is examined to reveal the underlying mechanisms governing low-temperature toughness. The findings of this study can serve as a useful reference for the effective design and control of high-strength pipeline steel.

2. Experimental Procedure

The chemical compositions of the two experimental steel plates with varying Nb contents are listed in Table 1. The thick steel plates (thickness of 24 mm) were obtained by thermo-mechanical control processing (TMCP) after melting in a 120 kg vacuum furnace. A schematic of TMCP is shown in Figure 1. Firstly, a 140 mm thick ingot was heated to 1180 °C at a rate of 10 °C/s and held for 3 h. Then, the ingots were roughened to 70 mm in five passes at 1030–1050 °C and finally to 24 mm in six passes at 780–800 °C using a φ450 mm trial rolling mill. This was followed by accelerated cooling at 750 °C under an average cooling rate of 20 °C/s, which stopped at 420 °C. The measured TMCP parameters of the test steels are listed in Table 2.

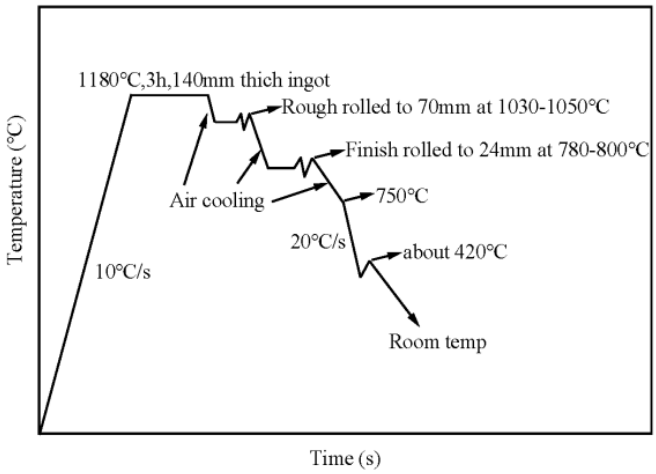

Figure 1. Schematic diagram of TMCP.

The microstructure of the steel plate samples was examined using metallographic microscopy (Axion-200MAT, ZEISS, Oberkochen, Germany) and scanning electron microscopy (SEM; S-3400N, HITACHI, Tokyo, Japan) after grinding, mechanical polishing, and etching with a 4% nitric acid–alcohol solution. For transmission electron microscopy (TEM; JEM-2010; JEOL Ltd., Tokyo, Japan), the thin film sample was polished to a thickness of 30 μm through multiple passes of sandpaper, then processed into a circular disc with a diameter

of 3 mm. Finally, the thin film sample was electropolished. The polishing solution was 5% perchloric acid in ethyl alcohol, with a polishing voltage of 25 V, current of 55–65 mA, and temperature of 25 °C. Image Pro Plus 6.3 (MEDIA, Rockville, MD, USA) software was used to randomly determine the content and size of the M/A constituents under 10 SEM fields of view. The area of the M/A islands in the SEM images was considered as the M/A constituent content, and the arithmetic mean values of area, length (L_{max}), and width (L_{min}) were taken as the average size of M/A components. The specimen was horizontally cut on a rolled plate and machined into a standard Charpy V-notch impact specimen with a size of 10 mm × 10 mm × 55 mm to conduct a low-temperature impact test on a JB-300B semi-automatic impact testing machine at −45 °C. The microstructure of the sample and the secondary cracks on the fracture section were analyzed using SEM (S-3400N) and electron backscatter diffraction (EBSD; EDAX, Mahwah, NJ, USA). The mean equivalent diameter (MED) of grains and the proportion of high-angle grain boundaries (HAGBs) were analyzed by EBSD analysis software (OIM Analysis 9; EDAX, Berwyn, PA, USA). The effect of microstructure on the impact toughness of X80 steel and the corresponding influence mechanism were also investigated. For EBSD analysis, the scanning step size was selected to be 0.2 μm. The size of the cleavage fracture surfaces was obtained by measuring the diameter of the equivalent circle of the cleavage surface using Image Pro Plus software. For obtaining accurate data, at least 50 cleavage surfaces were considered for each data point, then the average value was taken. The effect of Nb on the phase transformation of alloy steel was analyzed by a Gleeble 3500 thermal simulation test machine ((Dynamic Systems Inc., Poestenkill, NY, USA).

Table 1. Chemical compositions of each Nb-containing steel (wt.%).

Sample Name	C	Mn	P	S	Si	Ni	Cr	Cu	Mo	Nb	V	Ti	Carbon Equivalent Content (Ceq)	Crack Susceptibility Factor (Pcm)
0.05Nb	0.079	1.67	0.007	0.002	0.18	0.62	0.16	0.15	0.26	0.05	0.037	0.009	0.49	0.21
0.08Nb	0.070	1.70	0.006	0.002	0.16	0.66	0.15	0.15	0.25	0.08	0.034	0.008	0.47	0.202

CEN = C + f(C){Si/24 + Mn/6 + Cu/15 + Ni/20 + (Cr + Mo + Nb + V)/5 + 5B}, and f(C) = 0.75 + 0.25 tanh {20(C–0.12)}.

Table 2. TMCP parameters of test steel.

Steel	Heating Temperature (°C)	RRST (°C)	RRFT (°C)	FRST (°C)	FRFT (°C)	SCT (°C)	FCT (°C)	Cooling Rate (°C/s)
0.05Nb	1176	1091	1042	818	798	756	421	20
0.08Nb	1178	1088	1039	818	789	749	422	20

RRST—rough rolling start temperature; RRFT—rough rolling final temperature; FRST—finish rolling start temperature; FRFT—finish rolling final temperature; SCT—start cooling temperature; FCT—finish cooling temperature.

3. Results

3.1. Microstructure

The XRD patterns of the steel are shown in Figure 2. The results show that there were a large amount of ferrite (α) phases and a small amount of austenite (γ) phases in the steel. The volume fractions of retained austenite in the samples were determined by XRD; the retained austenite content in the 0.05Nb and 0.08Nb test steels was 0.83% and 1.1%, respectively. The metallographic and typical SEM images of the microstructure of the test steels with different Nb contents are shown in Figure 3a–d. The relative proportions of different microstructural constituents are presented in Figure 3e. The steel microstructure mainly contained PF, GB, LB, and M/A constituents. The microstructure of the sample with an Nb content of 0.05% primarily contained PF and GB, accounting for 12.5% and 85% of the total area, respectively, with the LB phase being relatively minor, occupying

only 2.5% of the area. When the Nb content increased to 0.08%, the LB phase became the primary constituent of the sample, occupying 81.8% of the microstructural area, while the proportions of GB and PF decreased to 3.6% and 14.6%, respectively.

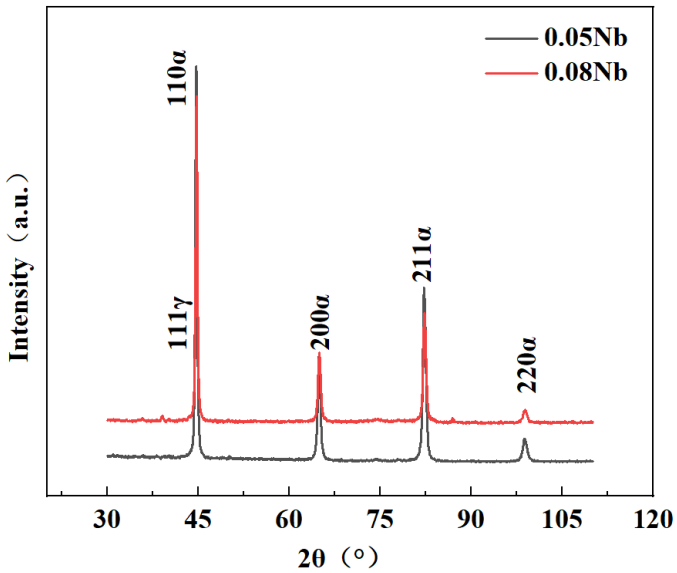

Figure 2. XRD patterns of the samples.

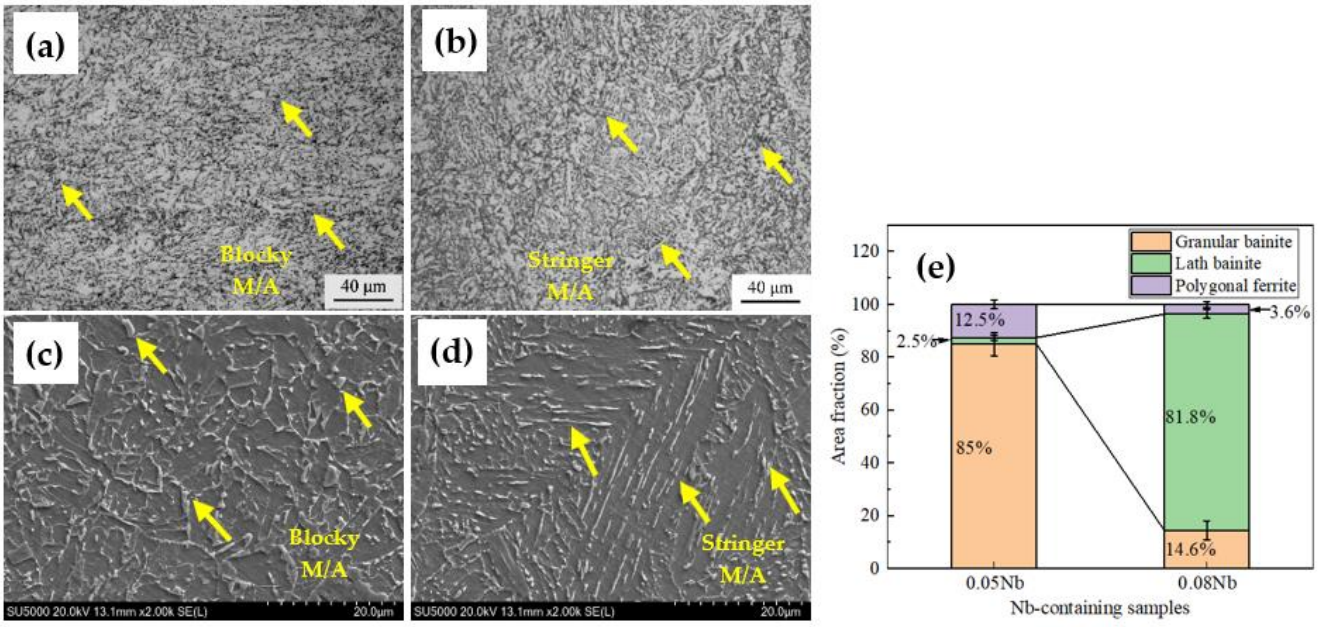

Figure 3. Metallographic and SEM images of the X80 steel specimens: (**a**,**c**) 0.05Nb; (**b**,**d**) 0.08Nb. (**e**) Quantitative statistical results for the samples with different Nb contents.

The statistical results for the proportion of M/A constituents are shown in Figure 4 and Table 3. With the increase in Nb content, the proportion of M/A constituents increased from 10.9% to 15.6%. The typical SEM images of M/A constituents reveal four different morphologies: islands (area < 5 μm^2, aspect ratio < 4), thin elongated shapes (area < 5 μm^2, aspect ratio > 4), thick elongated shapes (area > 5 μm^2, aspect ratio > 4), and block-like shapes (area > 5 μm^2, aspect ratio < 4), and the corresponding statistical results are presented in Table 3. With the increase in Nb content, the content of M/A constituents with elongated shapes significantly increased from 17.6% to 22.42%, while that of island-like M/A constituents decreased from 82.02% to 77.85%.

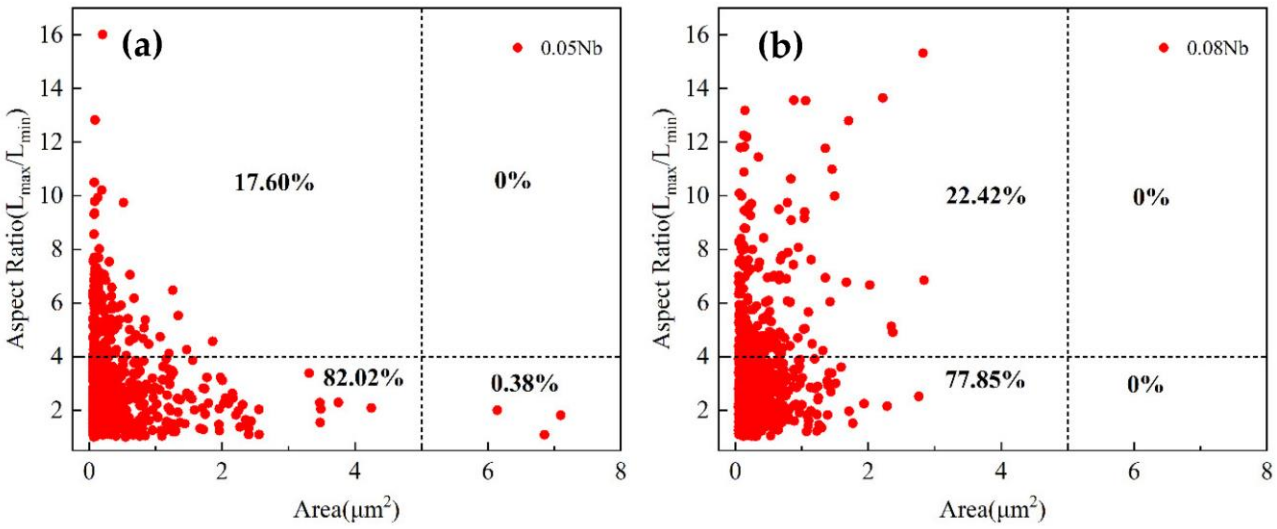

Figure 4. Quantitative statistics of M/A constituents in the steel samples with different Nb contents (**a**) 0.05Nb; (**b**) 0.08Nb.

Table 3. Quantitative statistics of M/A constituents in steels with different Nb contents.

Steel	M/A Content (Area %)	Island-like Shape (Number %)	Thin Elongated Shape (Number %)	Thick Elongated Shape (Number %)	Block-like Shape (Number %)
0.05Nb	10.9	82.0	17.6	0.4	0.0
0.08Nb	15.6	77.9	22.4	0.0	0.0

Figure 5 shows the TEM images of test steels with different Nb contents. The typical microstructure of AF, GB, LB, and M/A constituents can be observed in the figure. In addition, M/A constituents are observed in the bright-field images, dark-field images, and selected area electron diffraction (SAED) pattern (the diffraction spot (220)γ). The M/A constituents are dispersed between the bainite matrix with elongated or block-like shape. The TEM images indicate that an increase in Nb content leads to an increase in the LB content, a decrease in the GB content, an increase in the area fraction of M/A constituents, and the transformation of M/A constituents from block-like to elongated morphology, which is consistent with the SEM images. As shown in Figure 5f–h, the precipitated phase is mainly distributed in the granular bainite matrix with a certain dislocation density. The size of the precipitate is around 20–100 nm. Figure 5h clearly shows the presence of Nb–Ti-rich precipitate.

The EBSD images of test steels with different Nb contents are shown in Figure 6. The thick and thin lines in Figure 6 represent grain boundaries with different sizes and angles, and different colors represent different misorientation tolerance angles (MTAs). Specifically, the thick black lines represent MTA > 15°, while the thin white lines represent MTA = 2–15°.

Figure 7a shows the mean equivalent diameter (MED) of grains as a function of MTA for samples with different Nb contents. The equivalent grain size is the diameter of the equivalent circle enclosed by the grain boundaries with different MTAs. It can be seen that as the MTA increases, the MED also increases. As the Nb content increases, the equivalent grain size defined at each MTA decreases. Specifically, the MED corresponding to the MTA of 2–15° decreases from 3.86 ± 0.08 to 3.28 ± 0.11 μm, while the MED corresponding to MTA greater than 15° decreases from 4.43 ± 0.05 to 4.02 ± 0.09 μm.

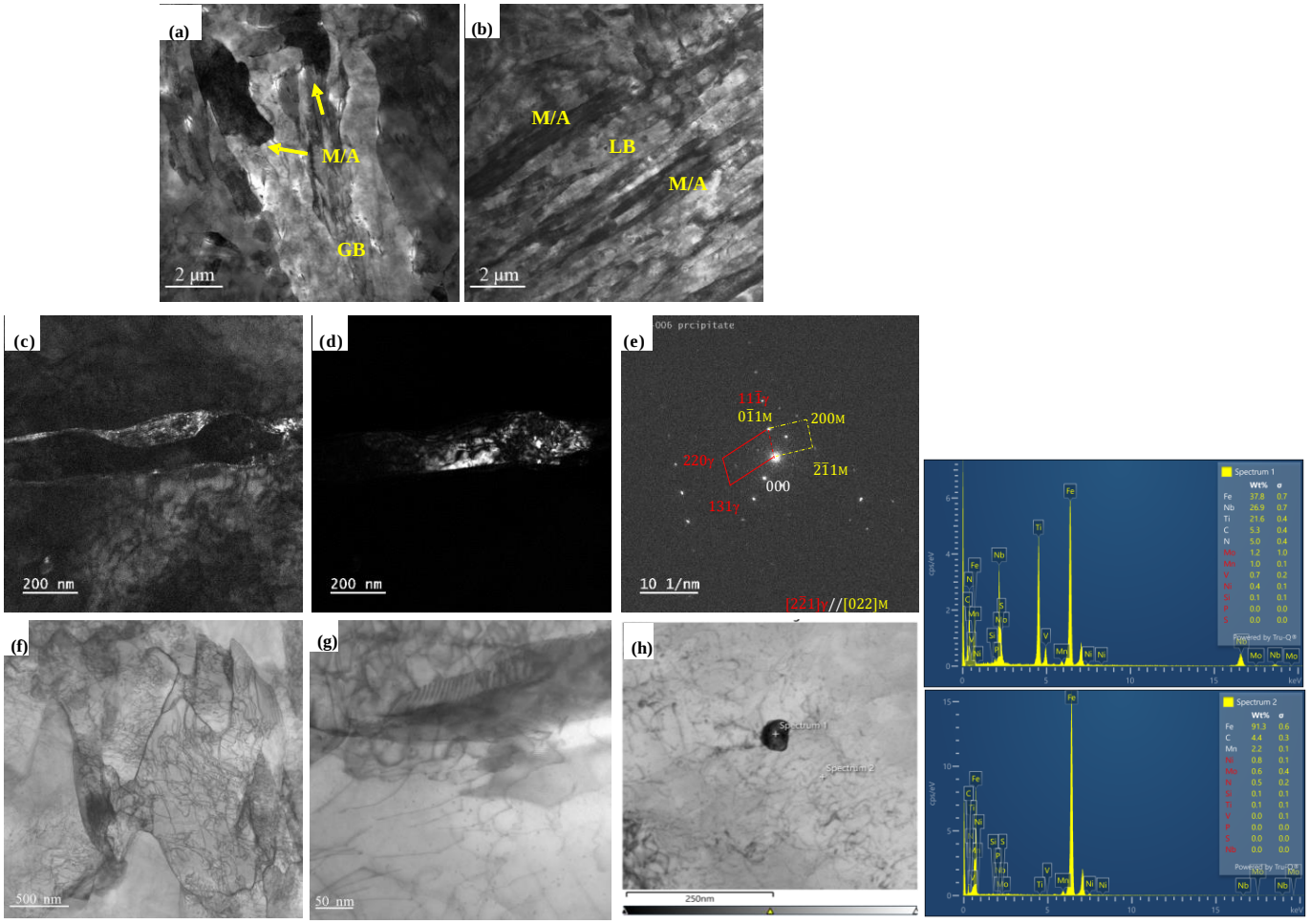

Figure 5. Typical TEM images of test steels with different Nb contents. (**a**) 0.05% Nb; (**b**–**e**) 0.08% Nb. (**c**) Bright-field image of the M/A constituents with elongated shape; (**d**) dark-field image of the M/A constituents (residual Austenite phase) with elongated shape; (**e**) corresponding selected area diffraction pattern. TEM bright-field (BF) image of the precipitate. (**f**) 0.05% Nb; (**g**,**h**) 0.08% Nb.

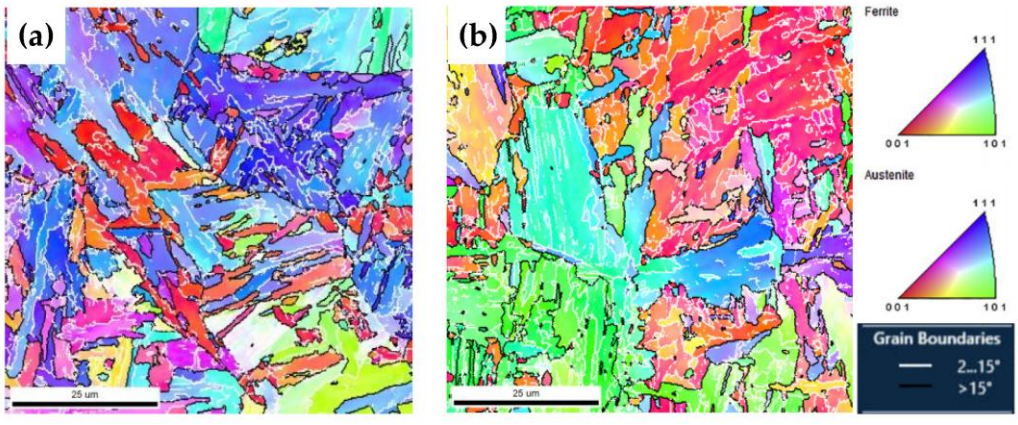

Figure 6. EBSD inverse pole figures of test steels with different Nb contents: (**a**) 0.05% Nb; (**b**) 0.08% Nb.

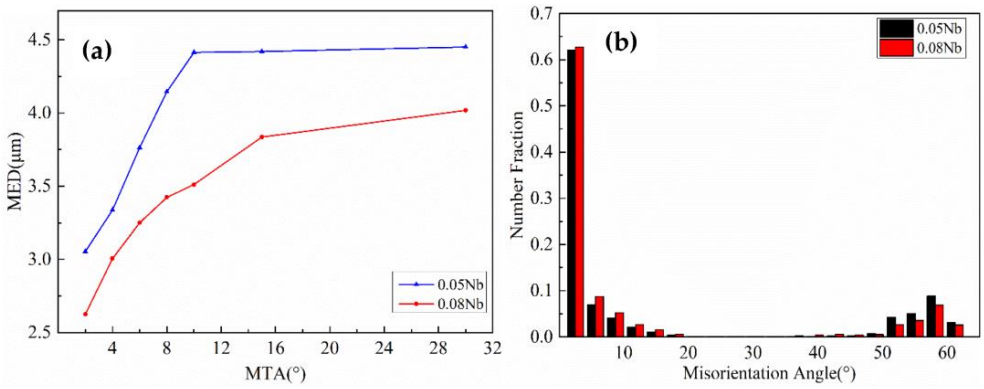

Figure 7. (**a**) Variation in the MED as a function of MTA for samples with different Nb contents. (**b**) Distribution of grain boundaries with different MTAs for different samples.

Figure 7b shows the proportion of grain boundaries with different MTAs in the test steels with different Nb contents. The proportion of low-angle grain boundaries (LAGBs) increases from 0.5 to 0.6, and that of HAGBs decreases from 0.5 to 0.4. Thus, as the Nb content increases, the proportion of HAGBs tends to decrease. The relevant statistical results are displayed in Table 4.

Table 4. Equivalent grain size and proportion of grain boundaries with different MTAs.

Steel	MED (μm)		Proportion of Grain Boundaries with Different MTAs (%)	
	2–15°	>15°	2–15°	15–65°
0.05Nb	3.86 ± 0.08	4.43 ± 0.05	0.5	0.5
0.08Nb	3.28 ± 0.11	4.02 ± 0.09	0.6	0.4

3.2. Impact Test

The load–displacement curves of 0.05Nb and 0.08Nb test steels at −45 °C are shown in Figure 8. The area of the enclosed region bounded by the vertical line to the left of the curve at the maximum load (Fm) in Figure 8 is the crack initiation energy, while the area of the enclosed region bounded by the vertical line to the right of the curve at Fm is the crack propagation energy. It can be seen in Table 5 that when the Nb content increases from 0.05 to 0.08, the crack initiation energy decreases from 83.5 J to 69.5 J, the crack propagation energy decreases from 133.5 J to 18.5 J, and the total impact energy decreases from 217 J to 88 J. The ratio of crack propagation energy to the total energy in the 0.08Nb test steel is relatively low, and after crack initiation, less energy is consumed in the crack propagation, resulting in a decrease in the proportion of fiber zone in the fracture surface as well as the low-temperature absorption energy.

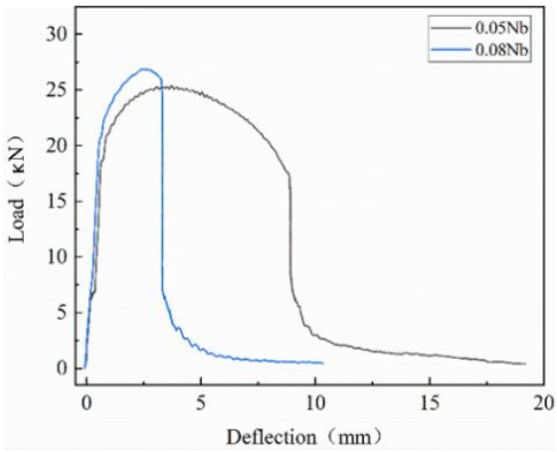

Figure 8. Load–displacement curves of the test steels with different Nb contents.

Table 5. Statistical results of the impact energy and cleavage fracture surface size.

Steel	Fm (kN)	E_i (J)	E_p (J)	E_t (J)	Cleavage Fracture Surface Size (μm^2)	The Percent Shear Fracture Area (SA, %)
0.05Nb	26.0	83.5	133.5	217.0	19 ± 2	41
0.08Nb	27.6	69.5	18.5	88.0	32 ± 2	11

Fm—Maximum load; E_i—Crack initiation energy; E_p—Crack propagation energy; E_t—Total impact energy.

Figure 9 shows the low-temperature impact fracture morphology of test steels with different Nb contents obtained by SEM at −45 °C. It includes both macroscopic (a,b) and microscopic (c–f) fracture morphologies, where (c,d) show the dimples in the fiber zone, and (e,f) show the river-like patterns in the radiation zone.

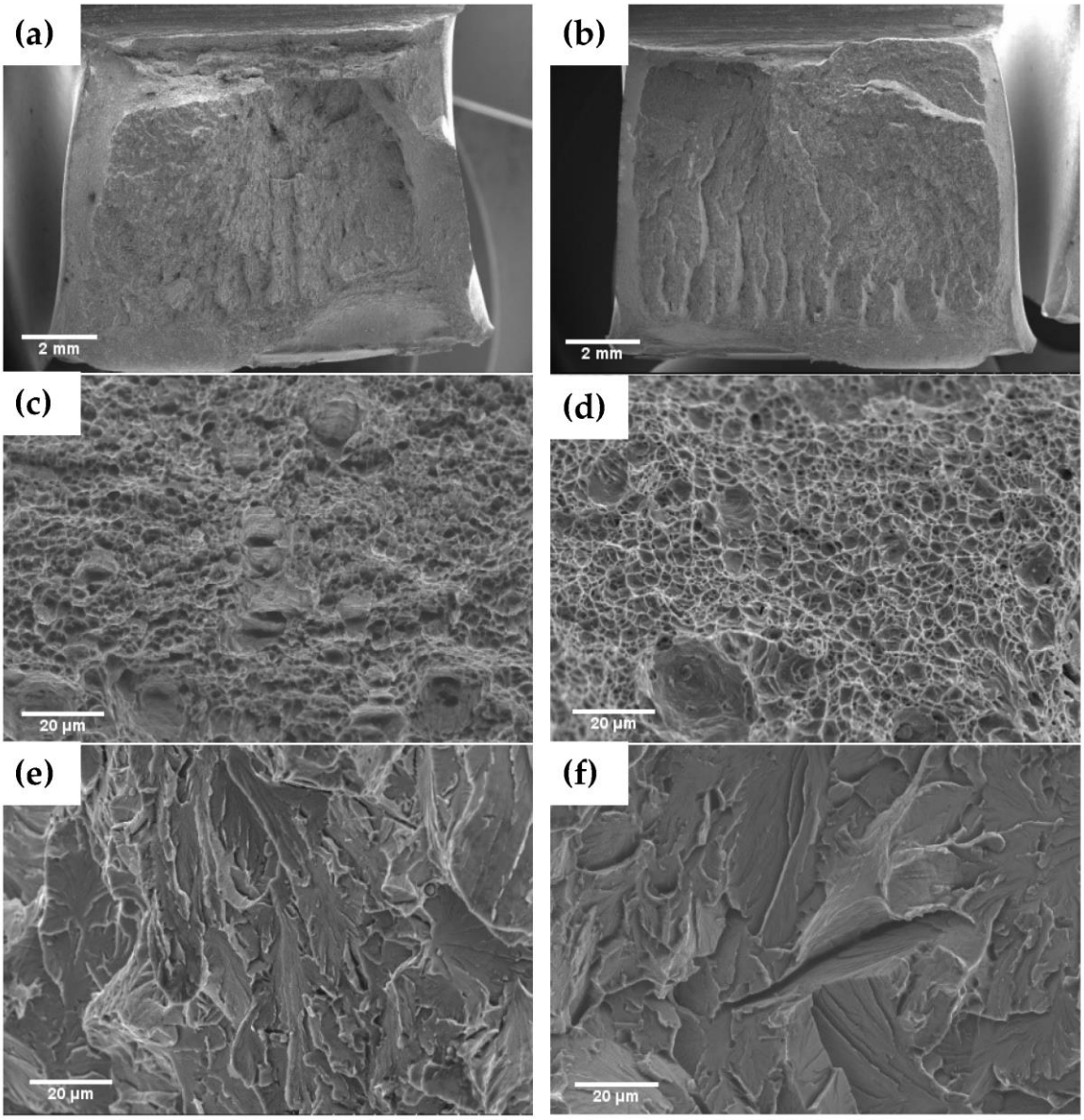

Figure 9. Low-temperature impact fracture surface images of the test steels with different Nb contents: (**a**,**c**,**e**) 0.05Nb; (**b**,**d**,**f**) 0.08Nb.

It can be observed that the size of the cleavage surface increases with the increase in Nb content. The statistical results are shown in Table 5, and there is a good agreement

between the cleavage surface size and impact energy of standard specimens (AKV_2). When the Nb content was 0.05, the test steel mainly exhibited ductile fracture, with small and deep dimples in the fiber zone. In Figure 9e, there are many tearing edges in the dissociation plane, ultimately resulting in excellent low-temperature toughness of the test steel. When the Nb content increased to 0.08, the test steel mainly exhibited brittle fracture, and the proportion of the fiber zone decreased. As shown in Figure 9d, the ductile dimples appear large and shallow. In Figure 9f, obvious secondary cracks extending directly into the radiation zone are observed, and the overall proportion of the fiber zone decreases. Consequently, the low-temperature impact toughness of the test steel decreased.

3.3. Thermal Expansion Curve

Figure 10 shows the expansion curve for the cooling process of X80 test steel. The starting point of austenite-to-ferrite transformation during the 20 °C/s cooling process was marked using the standard tangent method, and the starting temperature of phase transformation (Ar_3) was obtained. It was observed that as the Nb content increased, Ar_3 decreased.

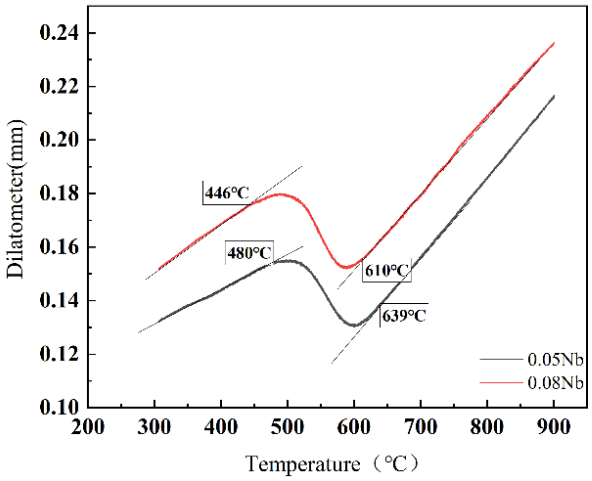

Figure 10. Thermal expansion curve of the test steels with different Nb contents.

4. Discussion

4.1. Effect of Nb Content on the Microstructural Evolution of Pipeline Steel

The mechanical properties of X80 pipeline steel are closely related to its microstructure. The content, shape, and size of the microstructure (GB + PF + LB + M/A mixed microstructure) significantly affect the low-temperature impact resistance of pipeline steel, as shown in Figures 4 and 8. As the Nb content increases, the amount of LB and M/A constituents increases, while the GB content decreases. Thus, the Nb content significantly governs the evolution of the mixed microstructure of X80 pipeline steel.

4.1.1. Effect of Nb Content on the Evolution of LB + GB + AF Mixed Microstructure

It has been reported that the formation temperature of GB is generally higher than that of LB, so GB nucleates first during the austenite cooling process [19]. The GB phase usually nucleates and grows at the prior austenite grain (PAG) boundaries, while the LB phase mainly nucleates inside the grains. As shown in Figure 10, when the Nb content increases from 0.05 to 0.08, Ar3 decreases from 639 to 610 °C, and the initial temperature of the $\gamma \rightarrow \alpha$ phase transition decreases. Thermodynamic analysis shows that the driving force promoting the nucleation and growth of LB increases, while the nucleation and growth of GB are inhibited. Therefore, LB becomes the main phase in this case. In addition, due to the driving force of 0.08Nb steel, the nucleation rate of α phase is relatively high, so the microstructure of the test steel is refined, and the MED value decreases.

4.1.2. Effect of Nb Content on the Evolution of M/A Microstructure

As described in Section 3.1, a mixed structure composed of GB, AF, LB, and M/A was formed in the 0.05Nb and 0.08Nb test steels. During the continuous cooling process from Ar3 to Ar1, the $\gamma \rightarrow \alpha + \gamma'$ phase transformation occurred in the test steel. Because C has much lower solubility in α than in γ phase, carbon atoms diffuse from ferrite to the surrounding austenite, leading to the formation of carbon-rich γ' phase [20,21]. As the Nb content increases, the phase transition occurs in the two-phase region (ferrite + austenite) and the carbon content of austenite phase increases. The concentration of carbon continues to increase, and the resistance to further transformation increases. Further, the phase stability improves, and the residual austenite content at room temperature increases. The final residual carbon-rich γ' further transforms into an M/A constituent, and different phase transition processes alter the microstructure and internal substructure of the M/A [22]. As the Nb content increases, the proportion of M/A constituents increases and hinders the generation of island-like M/A constituents, as shown in Figures 3–5 and Table 3.

4.2. Effect of Nb Content on the Impact Behavior of Pipeline Steel

According to classical fracture theory [23,24], cracks are formed when the stress reaches a certain critical value. The critical fracture stress is related to the Young's modulus, effective surface energy, and M/A constituents. The M/A constituents have a high mechanical strength and hardness due to their high lattice distortion and dislocation density. There is a large difference in the strength and hardness between the M/A constituents and the surrounding bainitic ferrite matrix in pipeline steel, which has a significant impact on the crack initiation and propagation process. During the severe deformation process in the impact experiment, the crack generally formed near the M/A constituents due to the accumulation of high dislocation density between the hard phase M/A and the surrounding soft phase. When the impact strain is transferred to the structure, the soft bainitic ferrite phase in the structure first undergoes plastic deformation. At the same time, dislocation accumulation occurs at the interface between the matrix and mixed structure, especially at the M/A constituents and the surrounding interfaces [25]. When the stress increases to the critical stress, microcracks nucleated by the M/A constituents propagate. This process can be quantitatively described using the Griffith local cracking model as follows:

$$\sigma_c = \left(\frac{2E\gamma_s}{\alpha a} \right)^{\frac{1}{2}}$$

where σ_c is the critical stress, E is the Young's modulus, γ_s is the effective surface energy of the interface fracture between the M/A constituents and the bainitic matrix, α is a constant related to the crack shape, and a is the size of the microcrack nucleating at or around the M/A constituents.

According to the above equation, the large M/A constituents can lead to the formation of microcracks, while small island-shaped M/A constituents can not only increase the critical stress but also effectively hinder the generation and propagation of secondary cracks. The small size of the M/A constituents in the test steel with low Nb content results in a higher critical stress, leading to a higher crack initiation energy. Consequently, with the increase in Nb content, the content and size of M/A constituents increase, leading to a decrease in the critical stress. In addition, cracks can more easily propagate along or through these elongated M/A components, as shown in Figure 11.

The 0.05Nb test steel sample was cut along the center of the plane perpendicular to the fracture surface, and the typical secondary crack morphology was observed through SEM. The results are shown in Figure 11. The micropores in the matrix tend to nucleate at the carbides or small M/A constituents through particle fracture or particle/matrix interface detachment, as shown in Figure 11a. Such micropores require a huge amount of energy to aggregate and grow in the plastic deformation zone [26–29]. When the secondary cracks propagate in the radiation zone of the sample, they encounter HAGBs and small block-like

M/A constituents, leading to bending and even fracture termination. The HAGBs or small M/A constituents can hinder crack propagation, which is conducive to improving the impact performance of the sample.

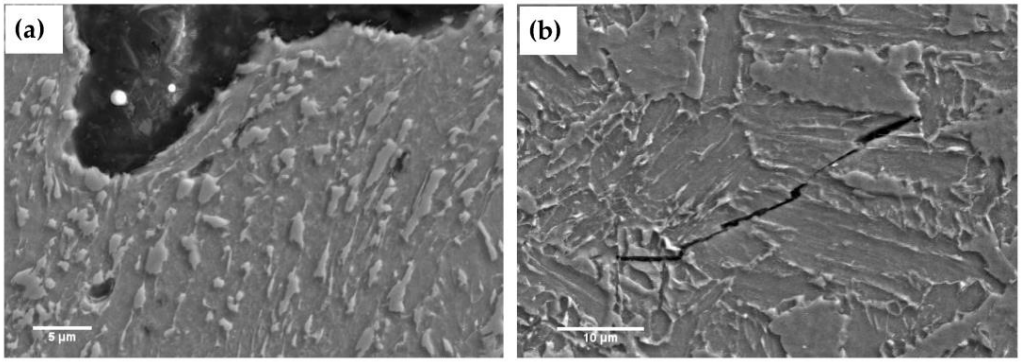

Figure 11. SEM images of the secondary cracks and microcracks in the test steels with different Nb contents: (**a**) 0.05Nb; (**b**) 0.08Nb.

The deflection or termination of crack propagation largely depends on the crystal orientation relationships between the sub-structures through which the crack passes, between the substructures and grains, and between the grains [26]. When the crack propagation process is accompanied with energy consumption or the formation of small plastic deformation zones, these interfaces can hinder the crack propagation.

Some grain boundaries can suppress the crack propagation, which is usually accompanied by energy consumption or the formation of small plastic deformation zones [27–29]. According to the inverse pole figure maps of the fracture surface of pipeline steel in Figure 12a,b, cracks cannot deflect or stop at the LAGBs, but the propagation of secondary cracks is affected by the HAGBs. Therefore, during the impact loading process, HAGBs can hinder the propagation of cracks and improve the impact propagation energy of pipeline steel. The high-density HAGBs enhance the impact toughness of pipeline steel. It is evident from Figure 9 and Table 4 that when the Nb content increases from 0.05% to 0.08%, the content of HAGBs in the test steel decreases from 52.7% to 35.4%. As shown in Figure 12b, cracks propagate almost linearly within the grains until they stop at the PAG boundary. In the test steels with high Nb content, the reduction in these obstacles encountered during the crack propagation greatly reduced the energy required for crack propagation, thereby promoting the crack propagation process.

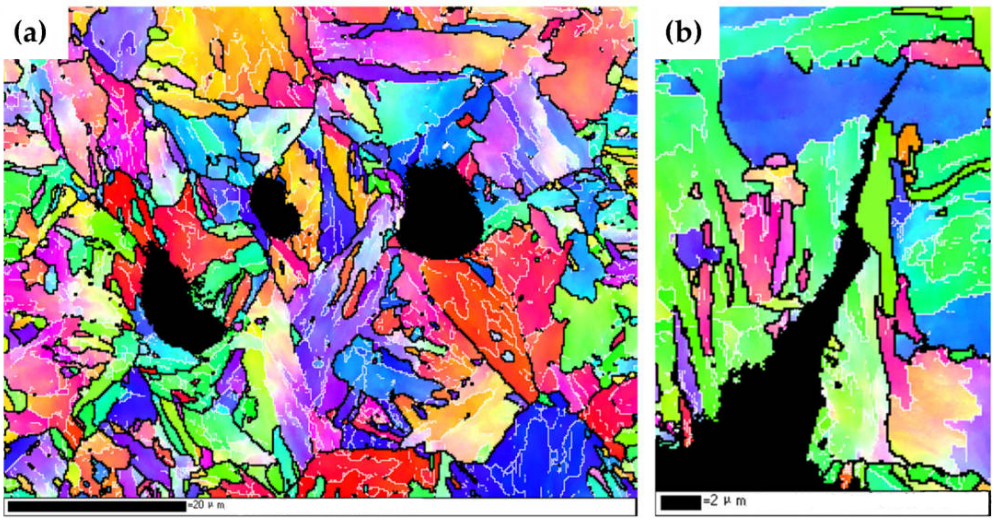

Figure 12. EBSD inverse pole figures of the secondary cracks and microcracks in the test steels with different Nb contents: (**a**) 0.05Nb; (**b**) 0.08Nb.

5. Conclusions

The effect of Nb content on the phase transformation, impact toughness, and microstructure of X80 grade pipeline steel was examined using metallographic microscopy, SEM, EBSD, TEM, and impact testing. The main results of this study are summarized as follows:

(1) The microstructure of X80 pipeline steel mainly included AF, PF, LB, GB, and M/A constituents. With the increase in the Nb content, the microstructure was refined. The MED corresponding to MTA greater than 15° reduced from 4.43 ± 0.05 to 4.02 ± 0.09 μm. At the same time, the content of GB and AF in the microstructure decreased, while that of LB and M/A constituents increased. With the increase in the Nb content from 0.05 to 0.08 wt.%, the proportion of M/A constituents increased from 10.9% to 15.6%

(2) As the Nb content increased from 0.05 to 0.08 wt.%, the crack initiation energy decreased from 83.5 J to 69.5 J, the crack propagation energy decreased from 133.5 J to 18.5 J, and the total impact energy decreased from 217 J to 88 J. In addition, the fracture mode changed from mixed fracture to cleavage fracture.

(3) The content and shape of M/A constituents and the volume fraction of HAGBs significantly affected the low-temperature toughness of pipeline steel. A small amount of small-sized block-like M/A constituents and a high-volume fraction of HAGBs were found to significantly improve the low-temperature impact toughness of the tested pipeline steel.

Author Contributions: Q.W. and J.J. conceived and designed the experiments; Z.Z. and L.Y. performed the experiments; K.G. analyzed the data and critically revise the main problems of the article; Y.G. contributed in the experimental material and analysis tools; Y.G. supervised this paper; and Q.W. and J.J. wrote the paper; Q.W. and Y.G. are responsible for final approval of the version to be published. All authors have read and agreed to the published version of the manuscript.

Funding: This work was funded by the National Key Research and Development Program of China (Grant No. 2017YFB0304800 and Grant No. 2017YFB0304802 for the second subproject), and the Key Research and Development Program between Nanjing Iron & Steel United Co., Ltd. and Yanshan University (Grant No. IGAB19060004).

Data Availability Statement: The data presented in this study are available in article.

Conflicts of Interest: Author Jinxing Jiang was employed by the company Plate Business Department, Nanjing Iron & Steel United Co., Ltd. The remaining authors declare that the research was conducted in the absence of any commercial or financial relationships that could be construed as a potential conflict of interest.

References

1. Sharma, S.K.; Maheshwari, S. A review on welding of high strength oil and gas pipeline steels. *J. Nat. Gas Sci. Eng.* **2016**, *38*, 203–217. [CrossRef]
2. Buzzichelli, G.; Anelli, E. Present status and perspectives of European research in the field of advanced structural steels. *ISIJ Int.* **2007**, *42*, 1354–1363. [CrossRef]
3. Khalaj, G.; Pouraliakbar, H.; Kaveh, R.M.; Khalaj, M.-J. Modeling the correlation between heat treatment, chemical composition and bainite fraction of pipeline steels by means of artificial neural networks. *Neural Netw. World J.* **2013**, *23*, 351–367. [CrossRef]
4. Khalaj, G.; Yoozbashizadeh, H.; Khodabandeh, A.; Tamizifar, M. Austenite grain growth modelling in weld heat affected zone of Nb/Ti microalloyed linepipe steel. *Mater. Sci. Technol.* **2014**, *30*, 424–433. [CrossRef]
5. Folga, S.M. *Natural Gas Pipeline Technology Overview*; Technical Report; U.S. Department of Energy Office of Scientific and Technical Information: Oak Ridge, TN, USA, 2007.
6. Zhou, F.; Gao, Z.; Wu, K.M. Effect of Nb content on the impact toughness of coarse-grained heat-affected zone of pipeline steels under large heat input. *Adv. Mater. Res.* **2015**, *1078*, 3–7. [CrossRef]
7. Chen, X.W.; Qiao, G.Y.; Han, X.L.; Wang, X.; Xiao, F.R.; Liao, B. Effects of Mo, Cr and Nb on microstructure and mechanical properties of heat affected zone for Nb-bearing X80 pipeline steels. *Mater. Des.* **2014**, *53*, 888–901. [CrossRef]
8. Kim, Y.M.; Kim, S.K.; Lim, Y.J.; Kim, N.J. Effect of Microstructure on the Yield Ratio and Low Temperature Toughness of Pipeline Steels. *ISIJ Int.* **2002**, *42*, 1571–1577. [CrossRef]

9. Sun, X.; Zhou, M.X.; Zhu, M.; Wang, H.; Zhang, Q.; Tian, J.; Xu, G. Microstructure and mechanical properties of Nb microalloyed high-carbon pearlitic steels subjected to isothermal transformation. *Mater. Charact.* **2023**, *202*, 113013.
10. Bai, P.H.; Shang, C.L.; Wu, H.H.; Ma, G.; Wang, S.; Wu, G.; Gao, J.; Chen, Y.; Zhang, J.; Zhu, J.; et al. A review on the advance of low-temperature toughness in pipeline steels. *J. Mater. Res. Technol.* **2023**, *25*, 6949–6964. [CrossRef]
11. Wu, G.; Liu, C.; Chen, R.; Li, X.; Jiang, M. Effects of Alloy Content on Impact Toughness in X80 Pipeline Steel. In Proceedings of the International Forum on Electrical Engineering & Automation. 2016. Available online: https://api.semanticscholar.org/CorpusID:59462783 (accessed on 10 January 2016).
12. Chen, X.W.; Liao, B.; Qiao, G.Y.; Gu, Y.; Wang, X.; Xiao, F.R. Effect of Nb on Mechanical Properties of HAZ for High Nb X80 Pipeline Steels. *J. Iron Steel Res.* **2013**, *20*, 53–60. [CrossRef]
13. Garcia-Sesma, L.; Lopez, B.; Pereda, B. Effect of coiling conditions on the strengthening mechanisms of Nb microalloyed steels with high Ti addition levels. *Mater. Sci. Eng. A* **2019**, *748*, 386–395. [CrossRef]
14. Zhao, Y.T.; Shang, C.J.; Yang, S.W.; Wang, X.M.; He, X.L. The metastable austenite transformation in Mo–Nb-Cu-B low carbon steel. *Mater. Sci. Eng. A* **2006**, *433*, 169–174. [CrossRef]
15. Xia, F.; Li, Z.; Ming, M.; Zhao, Y.; Wu, C.; Su, X.; Peng, H. Effect of Nb on microstructure and corrosion resistance of X80 pipeline steel. International. *J. Press. Vessel. Pip.* **2023**, *203*, 104949. [CrossRef]
16. Shang, C.; Wang, X.; Zhou, Z.; Liang, X.; He, X. Evolution of intermediate transformation microstructures in Mn-Mo-Nb-B low carbon microalloyed steel. *Acta Metall. Sin.* **2008**, *44*, 287–291.
17. Pereda, B.; Fernandez, A.I.; Lopez, B.; Rodriguez-Ibabe, J.M. Effect of Mo on Dynamic Recrystallization Behavior of Nb-Mo Microalloyed Steels. *Trans. Iron Steel Inst. Jpn.* **2007**, *47*, 860–868. [CrossRef]
18. Zhang, F.; Xiang, C.; Han, E.H.; Zhang, Z. Effect of Nb Content on Microstructure and Mechanical Properties of Mo0.25V0.25Ti1.5Zr0.5Nbx High-Entropy Alloys. *Acta Metall. Sin.* **2022**, *35*, 12. [CrossRef]
19. Zhu, D.M.; He, J.L.; Shi, G.H.; Wang, Q.F. Effect of Welding Heat Input on the Microstructure and Impact Toughness of the Simulated CGHAZ in Q500qE Steel. *Acta Metall. Sin.* **2022**, *58*, 1581–1588.
20. Zhao, L.Y.; Wang, Q.F.; Shi, G.H.; Yang, X.; Qiao, M.; Wu, J.; Zhang, F. In-depth understanding of the relationship between dislocation substructure and tensile properties in a low-carbon microalloyed steel. *Mater. Sci. Eng. A* **2022**, *854*, 12. [CrossRef]
21. Fu, C.; Li, X.D.; Li, H.C.; Han, T.; Han, B.; Wang, Y. Influence of ICCGHAZ on the Low-Temperature Toughness in HAZ of Heavy-Wall X80 Pipeline Steel. *Metals* **2022**, *12*, 907. [CrossRef]
22. Zhang, Y.; Shi, G.H.; Sun, R.; Guo, K.; Zhang, C.; Wang, Q. Effect of Si content on the microstructures and the impact properties in the coarse-grained heat-affected zone (CGHAZ) of typical weathering steel. *Mater. Sci. Eng. A* **2019**, *762*, 10. [CrossRef]
23. Lan, L.; Qiu, C.; Zhao, X.D.; Gao, X.; Du, L. Microstructural characteristics and toughness of the simulated coarse grained heat affected zone of high strength low carbon bainitic steel. *Mater. Sci. Eng. A* **2011**, *529*, 192–200. [CrossRef]
24. Lee, S.G.; Sohn, S.S.; Kim, B.; Kim, W.G.; Um, K.-K.; Lee, S. Effects of martensite-austenite constituent on crack initiation and propagation in inter-critical heat-affected zone of high-strength low-alloy (HSLA) steel. *Mater. Sci. Eng. A* **2018**, *715*, 332–339. [CrossRef]
25. Xie, C.; Liu, Z.; He, X.; Wang, X.; Qiao, S. Effect of martensite–austenite constituents on impact toughness of pre-tempered MnNiMo bainitic steel—ScienceDirect. *Mater. Charact.* **2020**, *161*, 110139. [CrossRef]
26. Huda, N.; Wang, Y.Y.; Li, L.J.; Gerlich, A.P. Effect of martensite-austenite (MA) distribution on mechanical properties of inter-critical Reheated Coarse Grain heat affected zone in X80 linepipe steel. *Mater. Sci. Eng. A* **2019**, *765*, 9. [CrossRef]
27. Yang, Y.; Jia, X.; Ma, Y.; Wang, P.; Zhu, F.; Yang, H.; Wang, C.; Wang, S. Effect of Nb on microstructure and mechanical properties between base metal and high heat input coarse-grain HAZ in a Ti-deoxidized low carbon high strength steel. *J. Mater. Res. Technol.* **2022**, *18*, 2399–2412. [CrossRef]
28. Chen, J.; Tang, S.; Liu, Z.-Y.; Wang, G.-D. Microstructural characteristics with various cooling paths and the mechanism of embrittlement and toughening in low-carbon high performance bridge steel. *Mater. Sci. Eng. A* **2013**, *559*, 241–249. [CrossRef]
29. Goods, S.H.; Brown, L.M. Overview No. 1, The nucleation of cavities by plastic deformation. *Acta Metall.* **1979**, *27*, 1–15. [CrossRef]